

A Frequency-Domain Numerical Method for Noise Radiation from Ducted Fans

Y. Özyörük*, E. Alpman†

Department of Aerospace Engineering
Middle East Technical University, 06531 Ankara, Turkey

V. Ahuja‡

Combustion Research and Flow Technology, Inc.
Dublin, PA 18917, USA

L. N. Long§

Department of Aerospace Engineering
Pennsylvania State University, University Park, PA 16802, USA

Abstract

This paper describes a frequency-domain numerical method for predicting noise radiation from ducted fans, including acoustic treatment and nonuniform background flow effects. The method solves the Euler equations linearized about a mean flow in the frequency domain. A pseudo-time derivative term is added to the frequency-domain equations so that a time-marching technique can be employed to drive the acoustic field to steady state explicitly. This approach makes distributed parallel computing more viable for equations of this type and, although not implemented in the present work, allows use of well known convergence acceleration techniques from computational fluid dynamics, such as multigrid, to obtain the solutions efficiently. Simulations of the JT15D and a generic engine are shown at various operating conditions with comparison to results from time-domain studies and available experimental data.

* Assoc. Prof.

† Graduate Assistant, presently at the Department of Aerospace Engineering, Penn State University

‡ Research Associate

§ Professor, Assoc. Member, AIAA

Copyright©2002 by Y.Özyörük. Published by the American Institute of Aeronautics and Astronautics, Inc., with permission.

1 Introduction

More stringent regulations are being put forward to limit the emitted noise from aircraft, as the air traffic is increasing and the engine sizes are becoming increasingly larger. In fact, today ultra bypass ratio turbofan engines are being built which are as large as more than two meters in diameter. This makes the fan related component of engine noise extremely important. Reducing this component relies heavily on acoustic treatment (liners) of the ducting system of the engine. Selection of an appropriate lining material and determining its installation location requires detailed analysis of the sound fields of the engine inlet and exhaust ducts and their radiated noise.

Various approaches have appeared in the literature to predict fan noise. Eversman and his co-workers developed a finite-element code based on the Galerkin method [1, 2]. Later, they included acoustic treatment effects in their numerical model [3] and extended it to calculate both fore and aft radiation [4]. Hence this code became widely used (e.g. Ref. [5]). Eversman's code is based on the solution of the velocity potential equation in the frequency-domain including nonuniform background flow effects. This code used the wave envelope technique to find

far-field sound in its early developments [2] but later a Kirchhoff integration technique was incorporated into it [6]. The aft radiation version of this code models the shear-layer emanating from the shroud for including its refraction effects on sound propagation based on some kinematic approximations. Direct time-domain approaches [7, 8, 9, 10, 11, 12] have also appeared in parallel to the rapid progress in computational aeroacoustics. One important advantage of time-domain methods is the ability to handle multi-frequency sources in one single simulation. Nonlinear effects are also accounted for in time-domain methods through the solution of the full Euler or Navier-Stokes equations. Özyörük and Long [7] developed a parallel, 3-D Euler solver to predict forward-radiated noise of ducted fans. Later, Özyörük[13] extended this solver to include acoustic treatment effects. Hence, with the continuing work of the present authors time-domain methods have become quite mature including many realistic effects.

The goal of this paper is twofold. The first is to develop a parallel, frequency-domain code that includes the effects of nonuniform background flows and acoustic treatment. This code resorts only to the linearization of the Euler equations about a mean flow that comes from computational fluid dynamics (CFD) solutions, so that its refraction effects on sound propagation are included in computations more realistically. This is particularly important for aft radiation from turbofans, where the shear layer emanating from the shroud of the engine causes significant refraction of the emitted sound waves. The other goal is to write an equivalent code to the ongoing time-domain code development for aft radiation, with the same underlying equations and background flow treatment so that comparisons with the time-domain results are on the same grounds and with minimal approximations for linear problems.

The present approach is described in the next section. Although work is also continued to solve aft radiation problems, in the present paper only forward radiation simulations are presented. Calculations are performed for the JT15D engine inlet and a generic inlet and compared to available solutions and experimental data. It is demonstrated

that the developed code is capable of making accurate forward radiation predictions.

2 Mathematical Model

2.1 Governing Equations

The 3-D, time-dependent, linearized Euler equations are transformed into the frequency domain assuming perturbations of the primitive dependent variables are of the form

$$\mathbf{Q}'(\mathbf{x}, t) = \text{Re}\{\hat{\mathbf{Q}}(x, r, \omega) e^{i\omega t + im\theta}\} \quad (1)$$

where

$$\begin{aligned} \mathbf{Q}' &= [u', v', w', p']^T, \\ \hat{\mathbf{Q}} &= [\hat{u}, \hat{v}, \hat{w}, \hat{p}]^T, \end{aligned} \quad (2)$$

and $i = \sqrt{-1}$; u', v', w' are the velocities in the cylindrical x, r, θ coordinate directions, respectively; p is the pressure; and a hat on a variable indicates a complex quantity. In Eq. (1) ω is the circular frequency and the integer m represents the azimuthal mode number.

Upon substitution of Eq. (1) into the Euler equations linearized about a nonuniform, axisymmetric flow, in cylindrical coordinates the equations governing the amplitudes of the complex flow perturbations become

$$\begin{aligned} i\omega\hat{u} + u_0\frac{\partial\hat{u}}{\partial x} + v_0\frac{\partial\hat{u}}{\partial r} + \hat{u}\frac{\partial u_0}{\partial x} + \hat{v}\frac{\partial u_0}{\partial r} \\ + \frac{1}{\rho_0}\frac{\partial\hat{p}}{\partial x} - \frac{\hat{p}}{\rho_0^2 c_0^2}\frac{\partial p_0}{\partial x} = 0 \end{aligned} \quad (3)$$

$$\begin{aligned} i\omega\hat{v} + u_0\frac{\partial\hat{v}}{\partial x} + v_0\frac{\partial\hat{v}}{\partial r} + \hat{u}\frac{\partial v_0}{\partial x} + \hat{v}\frac{\partial v_0}{\partial r} \\ + \frac{1}{\rho_0}\frac{\partial\hat{p}}{\partial r} - \frac{\hat{p}}{\rho_0^2 c_0^2}\frac{\partial p_0}{\partial r} = 0 \end{aligned} \quad (4)$$

$$i\omega\hat{w} + u_0\frac{\partial\hat{w}}{\partial x} + v_0\frac{\partial\hat{w}}{\partial r} + \frac{im}{\rho_0 r}\hat{p} - \frac{v_0\hat{w}}{r} = 0 \quad (5)$$

$$\begin{aligned} i\omega\hat{p} + u_0\frac{\partial\hat{p}}{\partial x} + v_0\frac{\partial\hat{p}}{\partial r} + \hat{u}\frac{\partial p_0}{\partial x} \\ + \hat{v}\frac{\partial p_0}{\partial r} + \gamma p_0\left(\frac{\partial\hat{u}}{\partial x} + \frac{\partial\hat{v}}{\partial r} + \frac{\hat{v}}{r} + \frac{im}{r}\hat{w}\right) \\ + \gamma\hat{p}\left(\frac{\partial u_0}{\partial x} + \frac{\partial v_0}{\partial r} + \frac{v_0}{r}\right) = 0 \end{aligned} \quad (6)$$

where $[\rho_0, u_0, v_0, p_0]^T$ represent the nonuniform, aximymmetric flow states. Note that the above equations contain derivatives only in 2-D (x, r) and the periodic, azimuthal variations have been transformed only to source-like terms multiplied by im . Hence, the 3-D field of a single spinning mode needs to be solved only in the (x, r) coordinates, reducing the computational expense of full 3-D simulations greatly.

Equations (3-6) are transformed into a body-fitted curvilinear coordinate system through the mappings

$$x = x(\xi, \eta); r = r(\xi, \eta), \quad (7)$$

where (x, r) are the axial and radial coordinates, and (ξ, η) are the curvilinear coordinates.

2.2 Boundary Conditions

2.2.1 Fan-Face Conditions

Exact cylindrical duct eigensolutions are used at the fan face to excite the acoustic field, which is assumed to be a deviation from the mean field. Acoustic pressure at a constant x plane in a circular annular duct is given by

$$\hat{p}(r, \theta) = \sum_{m, \mu} A_{m\mu} [J_m(k_{m\mu}r) + Q_{m\mu} Y_m(k_{m\mu}r)] e^{i(m\theta)} \quad (8)$$

where m and μ are the azimuthal and radial mode orders, respectively; $A_{m\mu}$ is the amplitude of the (m, μ) mode; J_m and Y_m are the m th order Bessel functions of the first and second kind, respectively; $k_{m\mu}$ are the eigenvalues that make the transcendental equation zero resulting from the wall condition, $\partial\hat{p}/\partial r|_{wall} = 0$; $Q_{m\mu} = -J'_m(\sigma k_{m\mu})/Y'_m(\sigma k_{m\mu})$ in which a prime indicates a derivative with respect to r and σ is the hub-to-tip ratio. When there is no centerbody (i.e., $\sigma = 0$), $Q_{m\mu}$ is zero. The azimuthal mode order m is found using the rotor-stator interaction theory of Tyler and Sofrin [14]. According to this theory the circumferential mode order m is given by $m = nB + sV$, where B and V are the numbers of rotor blades and stator vanes, respectively, n is the time harmonic index and s is

any integer number. The number of rotor blades, number of exit guide vanes and the rotor speed are entered as part of the input to the code, and the modes that are cut-on are automatically determined based on the local mean flow conditions at the source plane, which is usually taken as the fan face. Outflow boundary conditions are applied at the source plane in conjunction with Eq. (8).

2.2.2 Hard-Wall Conditions

Consistent with the Euler equations fluid particles are let slip at a hard wall under the influence of pressure fluctuations. Numerically the normal component of the contravariant velocity perturbation is set to zero. That is, on an orthogonal mesh at the wall,

$$\hat{V}_C = \eta_x \hat{u} + \eta_r \hat{v} = 0 \quad (9)$$

The value of the tangential contravariant velocity perturbation $\hat{U}_C = \xi_x \hat{u} + \xi_r \hat{v}$ is extrapolated from the interior solution. The azimuthal velocity \hat{w} is also extrapolated from the interior solution. The pressure perturbation is then found from the normal momentum balance given as, assuming the grid lines are orthogonal at the wall,

$$\partial\hat{p}/\partial\eta = -[2\rho_0 v_{0,t} \hat{v}_t + (\hat{p}/c_0^2) v_{0,t}^2] \times [\eta_x^2 + \eta_r^2]^{-1/2} R^{-1} \quad (10)$$

where $v_{0,t}$ and \hat{v}_t are the mean tangential velocity and tangential velocity perturbation, respectively, c_0 is the local speed of sound ($c_0^2 = \gamma p_0/\rho_0$), and R is the radius of wall curvature, which may be found using the transformation metrics at the wall.

2.2.3 Impedance Condition

Acoustic impedance condition is applied on acoustically treated surfaces (liner). Because fluid particles are allowed to slip at a wall and because a non-zero normal velocity exists on an acoustic treatment panel, the same momentum equations as the interior are solved, but the energy equation is replaced with the impedance condition equation, given as [15]

$$i\omega \hat{p} + \mathcal{L}_0 \hat{p} = -i\omega Z(\omega) \hat{v}_n \quad (11)$$

where \hat{v}_n is the normal component of the velocity perturbation, $Z(\omega)$ is the frequency-dependent impedance. The spatial operator \mathcal{L}_0 of Eq. (11) is given in the curvilinear coordinates by

$$\mathcal{L}_0 = U_{0,C} \partial/\partial\xi + \nabla\eta \cdot \partial\mathbf{V}_0/\partial\eta \quad (12)$$

where ξ is the grid line along the surface, $U_{0,C}$ is the mean tangential contravariant velocity and \mathbf{V}_0 is the mean velocity. The last term of the \mathcal{L}_0 operator is neglected in the present paper since its value is usually small on low curvature surfaces.

The equation governing the normal velocity perturbation can be written at the wall as

$$i\omega\hat{v}_n + U_{0,C} \frac{\partial\hat{v}_n}{\partial\xi} + |\nabla\eta| \left[\frac{v_{0,n}}{\partial\eta} \hat{v}_n + \frac{1}{\rho_0} \frac{\partial\hat{p}}{\partial\eta} - \frac{\hat{p}}{\rho_0^2 c_0^2} \frac{\partial p_0}{\partial\eta} \right] + \frac{2v_{0,t}\hat{v}_t}{R} \quad (13)$$

where $v_{0,n}$ and $v_{0,t}$ are the mean normal and tangential velocities, respectively, and \hat{v}_t is the tangential velocity perturbation. Upon substitution of the normal velocity perturbation from Eq. (13) into Eq. (11), an equation governing the pressure perturbation along the lined surface is obtained in the following form:

$$A \frac{\partial^2 \hat{p}}{\partial \xi^2} + B \frac{\partial \hat{p}}{\partial \xi} + C \frac{\partial \hat{p}}{\partial \eta} + D \hat{p} + E = 0 \quad (14)$$

where

$$A = \frac{U_{0,C}^2}{i\omega Z} \quad (15)$$

$$B = \frac{U_{0,C}}{i\omega Z} \left[2i\omega + \frac{\partial U_{0,C}}{\partial \xi} + |\nabla\eta| \frac{\partial v_{0,n}}{\partial \eta} \right] \quad (16)$$

$$C = -|\nabla\eta|/\rho_0 \quad (17)$$

$$D = \frac{i\omega}{Z} + \frac{|\nabla\eta|}{Z} \frac{\partial v_{0,n}}{\partial \eta} + \frac{|\nabla\eta|}{\rho_0^2 c_0^2} \frac{\partial p_0}{\partial \eta} \quad (18)$$

$$E = -2v_{0,t}\hat{v}_t/R \quad (19)$$

Eq. (14) requires information of the tangential velocity perturbation. Therefore, the interior solution is obtained prior to the solution of this equation, so that the tangential velocity perturbation may be extrapolated to the soft wall from the interior solution.

2.2.4 Far-Field Conditions

Non-reflecting boundary conditions are solved on the exterior far-field boundaries. The boundary condition operator of Bayliss and Turkel [16] is used on the inflow boundary. This is similar to that proposed later by Tam and Webb [17]. At an outflow boundary, the linearized momentum equations are solved for the velocity perturbations, but the radiation operator is applied to the pressure perturbation as suggested by Ref. [17]. All far-field boundary conditions are also transformed to the frequency domain and recast in cylindrical coordinates so that the same mapping transformations as the interior apply to them.

2.3 Discretizations

A direct discretization of the governing equations and the far-field boundary conditions would result in a large linear system of equations in the complex unknowns \hat{u} , \hat{v} , \hat{w} , and \hat{p} . Solution of such equation systems is not usually efficient in distributed computing environments. The suitability of the explicit algorithms to parallel computing can, however, be exploited for solution of the present frequency-domain equations by introducing a pseudo time derivative to and discretizing them explicitly. This approach allows use of well known explicit time-integration methods and well known convergence acceleration techniques for rapid solutions of the equations of this type.

The interior and the far-field boundary equations are written in the form

$$\frac{d\hat{\mathbf{Q}}}{d\tau} + \mathbf{R}(\hat{\mathbf{Q}}) = 0 \quad (20)$$

where $\mathbf{R}(\hat{\mathbf{Q}})$ represents the semi-discretized governing equations and the far-field boundary conditions in curvilinear coordinates and the first term is the pseudo time-derivative term added to the equations. A four-stage Runge-Kutta time-integration scheme is employed to drive the solution to a steady harmonic state iteratively. Spatial derivatives are evaluated using fourth-order accurate finite differences in general but in the developed code second-order accurate differences are also available as an option. It should be

noted that since here the amplitudes of the perturbations are solved at a grid point, not their instantaneous values in time, the demand on discretization accuracy may be relaxed. Because central schemes lack of diffusion, artificial dissipation is used to suppress the development of spurious waves. A fourth-order, constant coefficient dissipation model was used in all the computations presented in the paper. The Runge-Kutta scheme is given by

$$\begin{aligned}
 \hat{\mathbf{Q}}^{(0)} &= \hat{\mathbf{Q}}^n, \\
 \hat{\mathbf{Q}}^{(1)} &= \hat{\mathbf{Q}}^n - \frac{1}{4} \Delta\tau [\mathbf{R}(\hat{\mathbf{Q}}^{(0)}) - \mathbf{D}(\hat{\mathbf{Q}}^{(0)})] \\
 \hat{\mathbf{Q}}^{(2)} &= \hat{\mathbf{Q}}^n - \frac{1}{3} \Delta\tau [\mathbf{R}(\hat{\mathbf{Q}}^{(1)}) - \mathbf{D}(\hat{\mathbf{Q}}^{(0)})] \\
 \hat{\mathbf{Q}}^{(3)} &= \hat{\mathbf{Q}}^n - \frac{1}{2} \Delta\tau [\mathbf{R}(\hat{\mathbf{Q}}^{(2)}) - \mathbf{D}(\hat{\mathbf{Q}}^{(0)})] \\
 \hat{\mathbf{Q}}^{n+1} &= \hat{\mathbf{Q}}^n - \Delta\tau [\mathbf{R}(\hat{\mathbf{Q}}^{(3)}) - \mathbf{D}(\hat{\mathbf{Q}}^{(0)})]
 \end{aligned} \tag{21}$$

where superscript n shows the iteration step, $\Delta\tau$ is the pseudo time step size from an iteration step to the next, and $\mathbf{D}(\hat{\mathbf{Q}})$ is artificial dissipation.

In the present work the solution is stored at the cell centers, rather than the nodal points on the mesh. As a result of this, the wall conditions are applied between a fictitious point inside the wall and the first interior grid point off the wall. This procedure requires interpolation of data to the wall points. Third-order interpolation is used for fourth-order accuracy. Extrapolations of tangential contravariant velocities to a wall are also done to third-order accuracy.

2.4 Far-Field Predictions

Far-field sound is computed using a modified version of the Kirchhoff method that was previously developed by the authors [7]. In this method the Kirchhoff formula given by Farassat and Myers [18] is integrated using a forward time-binning approach. At the end of a frequency-domain computation, a 3-D Kirchhoff surface is constructed by revolving a curve (a grid line or a set of grid lines) from the 2-D grid 360° around the engine axis and the computed acoustic data on this curve is discretely distributed over the constructed Kirchhoff surface for one wave period ac-

ording to Eq. (1). Then the discrete data on the Kirchhoff surface are integrated for specified far-field observer locations using the aforementioned Kirchhoff method.

2.5 Parallelization

Distributed computing approach is used in the present study. In this approach the computational grid is divided into smaller domains and each subdomain is assigned to a different processor that is on a network. The necessary data exchange across a shared boundary between two neighboring subdomains is realized via library routines from the Message Passing Interface (MPI) standard.

3 Results and Discussion

3.1 Radiation from the JT15D Inlet

The present method was tested considering first the small JT15D turbofan inlet that has been studied both computationally and experimentally [2, 19, 7]. This engine has a fan with 53.5 cm diameter and its hub-to-tip ratio is approximately 0.37, but the centerbody was neglected in the computations. Two different cases are presented here. These are the spinning (6,0) and (13,0) modes with and without acoustic treatment and with flow.

3.1.1 (6,0) mode

This mode was computed at a blade passing frequency (BPF) of 2100 Hz, a free-stream Mach number of 0.204, and a mass flow rate (\dot{m}) of 15 kg/s. The computational mesh was divided into 4 subdomains for parallel processing, as shown in Fig. 1. The pressure contours of the computed mean flow are also shown in this figure. It is clear that due to the deceleration of the flow at the leading edge of the inlet cowl, the mean pressure has increased values, while over the outside surface of the inlet the mean pressure has decreased values due to acceleration of the flow there. Such variations in the background flow cause refraction of acoustic waves, and therefore, must be taken

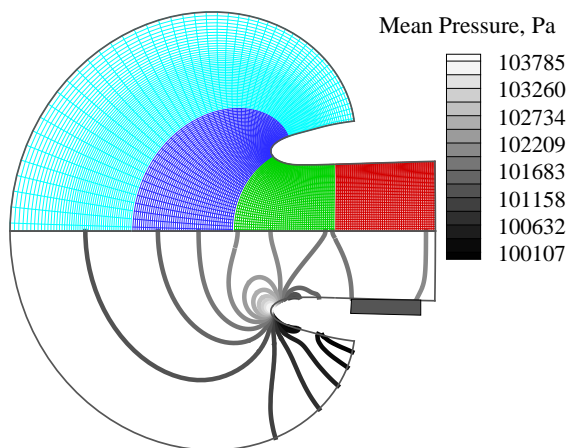


Figure 1: JT15D mesh and mean pressure contours: $M_\infty = 0.204$, $\dot{m} = 15$ kg/s.

into account properly for accurate radiation predictions.

Contours of the computed acoustic pressure amplitudes are shown in Fig. 2, upper half for the hard wall case and the lower half for a lined-wall case with specific resistance and reactance values of 4.01 and $-1.60i$, respectively. The liner length was taken as 24 cm and it was located as shown in Fig. 2. Sound absorbing effects of the liner are evident from the plotted contours of acoustic pressure amplitude. As indicated earlier, far-field predictions are realized through Kirchhoff surface integrations. For assessing the effect of the Kirchhoff surface placement on far-field predictions, three different Kirchhoff surfaces were considered. These are illustrated in Fig. 2. The integrations were performed for a 50-m radius arc from the inlet mouth. The resultant sound pressure levels (SPL) are shown in Fig. 3. A hard-wall flanged duct analytical solution [20] is also shown in the figure. Computations resulted the peak radiation at an angle of 49° from the inlet axis. The analytical solution was scaled to match the present solution at this angle. It is indicated by Fig. 3 that the computed results and the analytical solution are in good agreement for the radiated sound directivity. Also all the three Kirchhoff surface locations yielded nearly identical results. Consequently, Kirchhoff surface location II was chosen for the other JT15D calculations. Comparison of the SPL plots of the hard and soft-wall cases in-

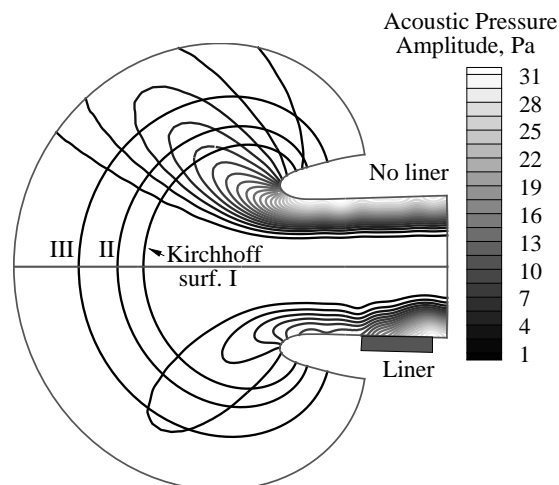


Figure 2: Contours of acoustic pressure amplitude for the JT15D inlet: Upper half without liner, lower half with liner having $Z/\rho_\infty c_\infty = 4.01 - 1.60i$. Source (6,0) mode at 2100 Hz, $M_\infty = 0.204$, $\dot{m} = 15$ kg/s.

dicates that the employed liner provided a 10.5 dB reduction in the peak radiation of the (6,0) mode at the specified frequency and flow conditions. The frequency-domain computations are also compared to the results of the time-domain code of Ref. [13] in Fig. 4. Hard-wall solutions given by both methods were matched at the peak radiation angle, and then the soft-wall solutions were plotted relatively. This was done since it was difficult to match the source plane amplitudes of both solutions. It is clear that the frequency-domain and time-domain directivities agree excellently for the hard-wall inlet, but about a 2-3 dB difference occurred between the soft-wall solutions of both methods.

3.1.2 (13,0) mode

The second test case considered involves the radiation of the (13,0) mode from the JT15D inlet at the same flow conditions as the preceding case. However, the BPF was set to 3150 Hz so that the computed results could be compared to the available experimental data of Heidelberg *et al.* [19]. At these conditions the mode cut-off ratio is 1.045. It is usually quite difficult to numerically capture and propagate acoustic waves that have cut-off

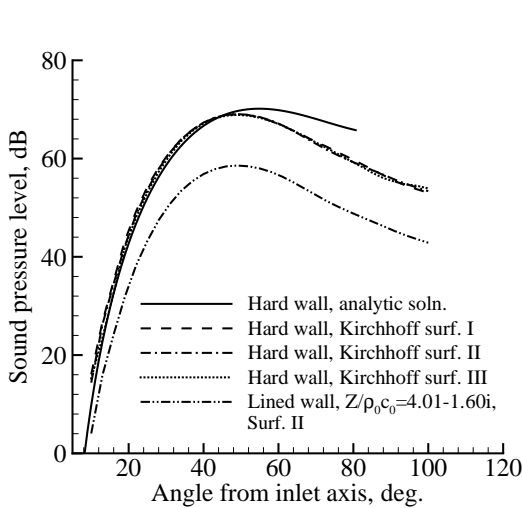


Figure 3: Far-field sound pressure levels of the JT15D inlet: Source (6,0) mode, BPF=2100 Hz, $M_\infty = 0.204$, $\dot{m} = 15$ kg/s.

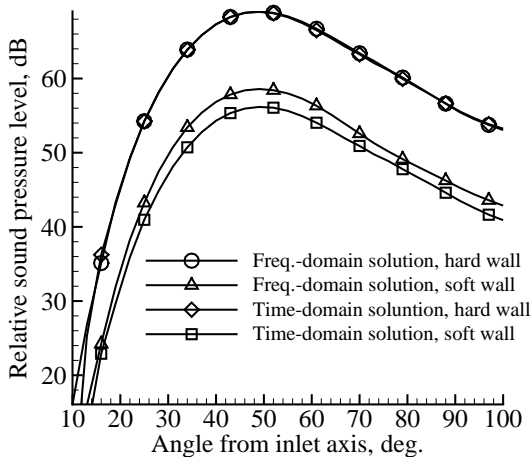


Figure 4: Comparison of the far-field solutions of the frequency and time-domain methods: JT15D inlet, source (6,0) mode, BPF=2100 Hz, $M_\infty = 0.204$, $\dot{m} = 15$ kg/s.

ratios close to unity. Therefore, to minimize numerical error build up, fourth-order discretization was used for the spatial derivatives. Also since the peak pressure value of the (13,0) mode occurs at the duct wall and the pressure decays relatively rapidly away from the wall, the centerbody was not considered to be important, although the experimental data of Ref. [19] was obtained with a centerbody. The liner had a length of 8 cm in the

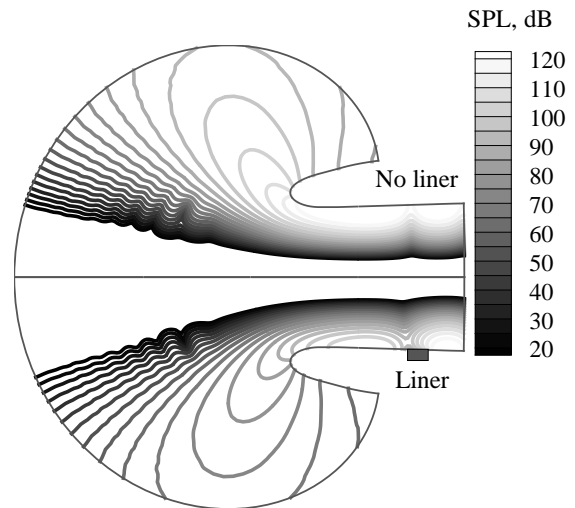


Figure 5: Contours of sound pressure level for the JT15D inlet: Upper half without liner, lower half with liner having $Z/\rho_\infty c_\infty = 0.638 + 0.5i$. Source (13,0) mode at 3150 Hz, $M_\infty = 0.204$, $\dot{m} = 15$ kg/s.

experiments, and it was located just upstream of the fan-face as shown for the present configuration in Fig. 5. However, it should also be noted that the experimental data of Ref. [19] were acquired at a static test condition (i.e. zero free-stream velocity) in which the mean Mach number reached about 0.147 at the source plane in the inlet. In the present computations the same mesh and the background flow as those used for the (6,0) mode of the preceding section were used (Fig. 1) and in this flow the mean Mach number reached about 0.168 at the source plane.

SPL contours of the computed acoustic field is shown in Fig. 5. The upper half shows the contours for the hard-wall case, while the lower half for the lined-wall with specific resistance and reactance values of 0.638 and 0.5, respectively. There appears to have occurred a standing wave in the duct resulting in a low acoustic pressure region just ahead of the fan face. This could be expected due to the reflections of the waves from the inlet mouth as a result of the changing sectional impedances due to the cross sectional area change. The sound attenuation effects of the liner is evident from the SPL contours shown in Fig. 5. The Kirchhoff surface location II of the preceding case

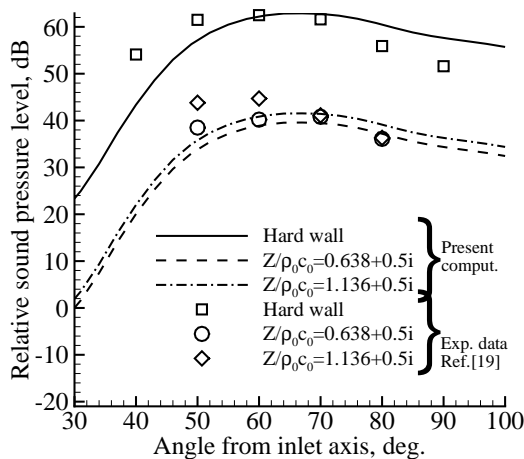


Figure 6: Far-field sound pressure levels of the JT15D inlet: Source (13,0) mode, BPF=3150 Hz, $M_\infty = 0.204$, $\dot{m} = 15$ kg/s.

was used for the far-field predictions, which are shown in Fig. 6 together with the experimental data of Ref. [19] for two different liner impedance values. It is clear that the present solution and the experimental data agree quite well on the general attenuation rates although the main lobe was predicted by the present method at a lower angle from the inlet axis. The shift to lower angles seen in the predictions of the directivity pattern of the far-field sound is probably because of the flow and geometry differences between the computations and experiment. In the static tests the flow just outside the nacelle was in the opposite direction than that in flight and away from the nacelle there was no flow at all. The above comparisons should be repeated with equivalent flow conditions and inlet geometry to the experiment to remove the shift in the predicted main lobe direction.

3.2 Radiation of (6,0) and (6,1) Modes from a Generic Engine

Computed results for far-field radiation from a generic engine inlet are presented in this section. This inlet has a diameter of 55.9 cm at the fan stage and the hub-to-tip ratio is 0.35. The free-stream Mach number and the mass flow rate are taken as 0.2 and 17.8 kg/s, respectively. With

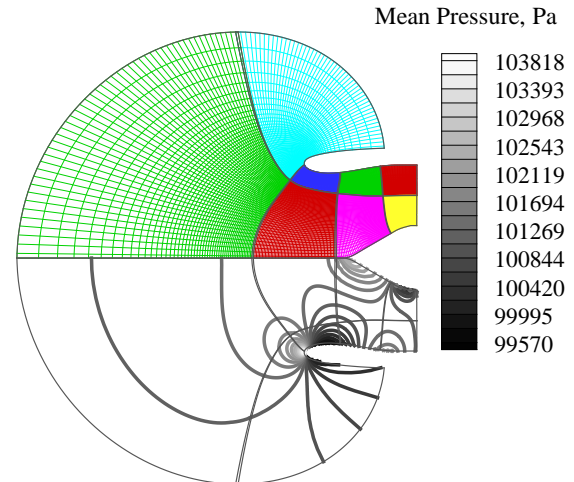


Figure 7: Generic engine mesh and the mean pressure contours: $M_\infty = 0.2$, $\dot{m} = 17.8$ kg/s.

the selected fan configuration and operating conditions, the spinning (6,0) and (6,1) modes are cut on at 2BPF, 3120 Hz. Unlike the results of the previous sections, the solutions were obtained with the centerbody of the engine. The amplitudes of the two modes were set such that their modal shapes were both multiplied by the same reference pressure.

The computational mesh and the mean flow pressure contours are shown together in Fig. 7. The acoustic field resulted from the (6,0)+(6,1) modes with an arbitrarily set 40 deg phase difference is demonstrated in Fig. 8. The upper half of the contours is for the hard-wall inlet and lower half for the lined inlet with a specific impedance value of $4.01 - 1.01i$. The liner location is also illustrated in this figure. It is clear that the acoustic fields of the hard and soft-wall inlets are very similar. In fact, only an insignificant attenuation was caused by this liner. This is illustrated in Fig. 9 in the far-field SPL plots of the (6,0)+(6,1) modes. Also shown in this figure are a hard-wall flunged duct analytical solution, soft-wall solution corresponding to the aforementioned location (denoted as position I in the figure) but with a specific impedance value changed to $2.17 - 1.98i$, and the solution with this impedance value but with liner location moved near the fan face (denoted as position II). The analytical solution and the present hard-wall solutions were matched at the

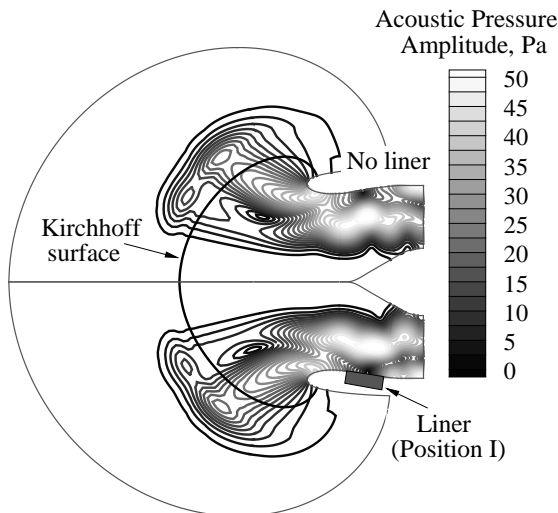


Figure 8: Contours of acoustic pressure amplitude for the generic inlet: Upper half without liner, lower half with liner having $Z/\rho_\infty c_\infty = 4.01 - 1.01i$. Source (6,0)+(6,1) modes with 45° phase difference, $2\text{BPF}=3120$ Hz, $M_\infty = 0.2$, $\dot{m} = 17.8$ kg/s.

peak SPL value of the radiated lobe that was predicted closer to the inlet axis. It is clear that the present solution and the analytical solution agree well on the shape of this lobe, but the peak value of the other lobe was underpredicted. This difference may be acceptable since the analytical solution is for a flunged, uniform duct and the flow speed through and outside the duct is assumed the same. It is interesting though the liner impedances and locations did not change the radiated sound field significantly. The reason for this can be better understood if the contours of the acoustic pressure amplitudes that are shown in Fig. 8 are examined more closely. It is clear that more intense sound field exists away from the inlet wall. This is due to the (6,1) mode itself and due to the cancellation or reinforcement of its sound field with that of the (6,0) mode. As a result the liner was not able to attenuate this (6,1) mode, which in turn dominated the far-field sound. As indicated above no relative scalings of the (6,0) and (6,1) modes were made.

In order to show how much the (6,0) mode component was actually attenuated by the liners, this mode was also considered alone. The resulting

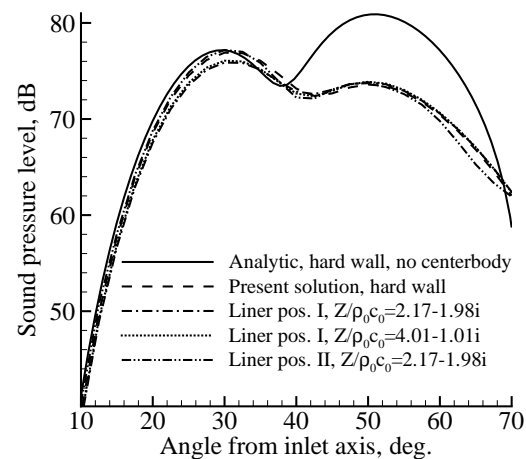


Figure 9: Far-field sound pressure levels of the generic engine: Source (6,0)+(6,1) modes with 45° phase difference, $2\text{BPF}=3120$ Hz, $M_\infty = 0.2$, $\dot{m} = 17.8$ kg/s.

acoustic field in the inlet is shown in Fig. 10 and the far-field SPL plots are shown in Fig. 11. It is clear that the present hard-wall solution and the corresponding flunged duct solution agree well for the (6,0) mode. It is also clear that the liner with a specific impedance value of $2.17 - 1.98i$ resulted more attenuation than that with a value of $4.01 - 1.01i$. Also the peak radiated SPL, which occurred around 32° from the inlet axis, was reduced by a value of about 6 dB by the former liner value, while this reduction remained limited to 4 dB by the latter one.

4 Convergence and Computational Performance

The developed code was run on a cluster of Pentium III, 700 MHz processors. Most of the runs required about 30 thousand steps for the acoustic field to converge. Each calculation took about 4-5 hrs. Although the convergence seems slow, we are expecting to be able to accelerate it by implementing a convergence acceleration technique, such as a multigrid method.

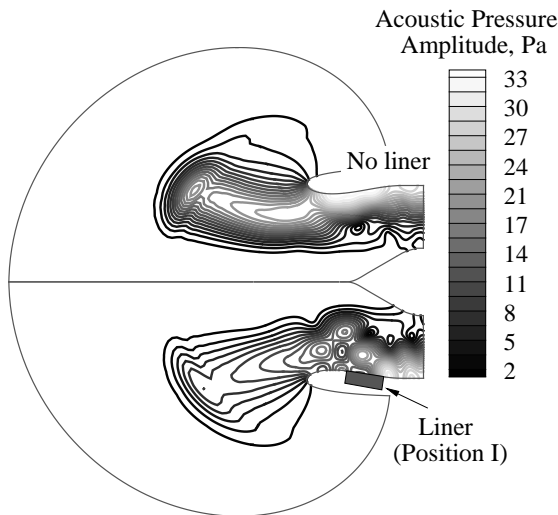


Figure 10: Contours of acoustic pressure amplitude for the generic inlet: Upper half without liner, lower half with liner having $Z/\rho_\infty c_\infty = 2.17 - 1.98i$. Source (6,0) mode only, 2 BPF=3120 Hz, $M_\infty = 0.2$, $\dot{m} = 17.8$ kg/s.

5 Conclusions

A frequency-domain method has been developed for predicting sound fields of ducted fans. The method is based on the solution of the frequency-domain form of the Euler equations linearized about an axisymmetric non-uniform background flow. Solutions are carried out employing an explicit pseudo time marching technique, which allows solutions of equations of this type on parallel computers. Although it has not been implemented yet, a well known convergence acceleration technique may readily be incorporated into the present approach due to its explicit nature. Example solutions were carried out for the JT15D engine inlet and for a generic engine at various conditions. It was demonstrated by comparing these simulations to available analytical solutions and experimental data that the developed method accurately predicts the forward arc far-field sound of ducted fans. The next step to the present work will be to incorporate a convergence acceleration technique and extend the method to aft radiation problems.

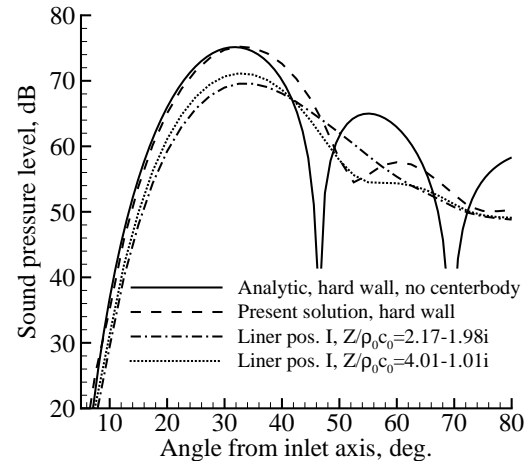


Figure 11: Far-field sound pressure levels of the generic engine: Source (6,0) mode only, 2 BPF=3120 Hz, $M_\infty = 0.2$, $\dot{m} = 17.8$ kg/s.

References

- [1] Astley, R. J., and Eversman, W. Wave envelope and finite element schemes for fan noise radiation from turbofan inlets. AIAA Paper 83-0709, 1983.
- [2] Eversman, W., Parrett, A. V., Preisser, J. S., and Silcox, R. J. Contributions to the finite element solution of the fan noise radiation problem. *Transactions of the ASME*, **107**, pp. 216-223, 1985.
- [3] Eversman, W., and Roy, I. D. Ducted fan acoustic radiation including the effects of nonuniform mean flow and acoustic treatment. AIAA Paper 93-4424, 1993.
- [4] Eversman, W. Aft fan duct acoustic radiation. CEAS/AIAA Paper 95-155, June 1995.
- [5] Nallasamy, M., Sutliff, D. L., and Heidelberg, L. J. Propagation of spinning acoustic modes in turbofan exhaust ducts. *Journal of Propulsion and Power*, **16(5)**, pp. 736-743, 2000.
- [6] Roy, I. D., and Eversman, W. Far-field calculations for turbofan noise. *AIAA Journal*, **39(12)**, pp. 2255-2261, December 2001.

- [7] Özyörük, Y., and Long, L. N. Computation of sound radiating from engine inlets. *AIAA Journal*, **34(5)**, pp. 894–901, May 1996.
- [8] Spence, P. L. Ducted fan noise prediction using wave envelope analysis and the Kirchhoff formula. AIAA Paper 97-1651-CP, *Proceedings of the 3th AIAA/CEAS Aeroacoustics Conference*, Atlanta, Georgia, USA, May 1997, pp.539–549.
- [9] Rumsey, C. L., Biedron, R. T., Farassat, F., and Spence, P. L. Ducted-fan engine acoustic predictions using a Navier-Stokes code. *Journal of Sound and Vibration*, **213(4)**, pp. 643–664, 1998.
- [10] Shim, I. B., Kim, J. W., and Lee, D. J. Numerical study on radiation of multiple pure tone noise from an aircraft engine inlet. AIAA Paper 99-1831, 5th AIAA/CEAS Aeroacoustics Conference and Exhibit, Bellevue, Washington, USA, May 1999.
- [11] Stanescu, D., Ait-Ali-Yahia, D., Habashi, W. G., and Robichaud, M. P. Multidomain spectral computations of sound radiation from ducted fans. *AIAA Journal*, **37(3)**, pp. 296–302, 1999.
- [12] Ahuja, V., Özyörük, Y., and Long, L. N. Computational simulations of fore and aft radiation from ducted fans. AIAA Paper 2000-1943, 6th AIAA/CEAS Aeroacoustics Conference and Exhibit, Hawaii, USA, June 2000.
- [13] Özyörük, Y. Parallel computation of forward radiated noise of ducted fans including acoustic treatment. *AIAA Journal*, **40(3)**, pp. 450–455, March 2002.
- [14] Tyler, J. M., and Sofrin, T. G. Axial flow compressor noise studies. *SAE Transactions*, **70**, pp. 309–332, 1962.
- [15] Myers, M. K. On the acoustic boundary condition in the presence of flow. *Journal of Sound and Vibration*, **71(3)**, pp. 429–434, 1980.
- [16] Bayliss, A., and Turkel, E. Far field boundary conditions for compressible flow. *Journal of Computational Physics*, **48**, pp. 182–199, 1982.
- [17] Tam, C. K. W., and Webb, J. C. Dispersion-relation-preserving finite difference schemes for computational acoustics. *Journal of Computational Physics*, **107**, pp. 262–281, 1993.
- [18] Farassat, F., and Myers, M. K. Extension of Kirchhoff's formula for radiation from moving surfaces. *Journal of Sound and Vibration*, **123**, pp. 451–460, 1988.
- [19] Heidelberg, L. J., Rice, E. J., and Homyak, L. Acoustic performance of inlet suppressors on an engine generating a single mode. AIAA Paper 81-1965, 1981.
- [20] Rice, E. J., and Heidmann, M. F. Modal propagation angles in a cylindrical duct with flow and their relation to sound radiation. AIAA Paper 79-0183, 1979.